1  From Continental Hyperextension to Seafloor Spreading: New Insights on the
2  Porcupine Basin from Wide-angle Seismic Data
3

4  **C. Chen[1, 2], L. Watremez[1, 3], M. Prada[4], T. Minshull[1], R. Edwards[2], B. O'Reilly[4], T.**
5  **Reston[5], G. Wagner[6], V. Gaw[6], D. Klaschen[6], and P. Shannon[7]**

6  [1]University of Southampton, Southampton, UK.
7  [2]National Oceanography Centre, Southampton, UK.
8  [3] Univ. Lille, CNRS, Univ. Littoral Côte d'Opale, UMR 8187, LOG, Laboratoire d'Océanologie
9  et de Géosciences, 59000 Lille, France
10  [4]Geophysics Section, Dublin Institute of Advanced Studies, Dublin, Ireland
11  [5]School of Geography, Earth and Environmental Sciences, University of Birmingham,
12  Birmingham, UK
13  [6]Geomar Helmholtz Centre for Ocean Research, Kiel, Germany
14  [7]School of Earth Sciences, University College Dublin, Dublin, Ireland
15

16  Corresponding author: Chen Chen (cc3g14@soton.ac.uk)

17  **Key Points:**

18  • New analysis of wide-angle seismic data from the southern Porcupine Basin.

19  • Evidence for presence of oceanic crust in the southern Porcupine Basin.

20  • Jurassic rifting propagated from south to north, resulting in non-uniform strain when
21  rifting stopped.
22

23    **Abstract**

24    The deep structure and sedimentary record of rift basins provide an important insight into

25    understanding the geological processes involved in lithospheric extension. We investigate the

26    crustal structure and large-scale sedimentary architecture of the southern Porcupine Basin,

27    offshore Ireland along three wide-angle seismic profiles, supplemented by thirteen selected

28    seismic reflection profiles. The seismic velocity and crustal geometry models obtained by joint

29    refraction and reflection travel-time inversion clearly image the deep structure of the basin. Our

30    results suggest the presence of three distinct crustal domains along the rifting axis: (a) continental

31    crust becoming progressively hyperextended from north to south through the basin, (b) a

32    transitional zone of uncertain nature and (c) a 7 - 8 km thick zone of oceanic crust. The latter is

33    overlain by a ~ 8 km compacted Upper Paleozoic-Mesozoic succession and ~ 2 km of Cenozoic

34    strata. Due to the lack of clear magnetic anomalies and in the absence of well control, the precise

35    age of interpreted oceanic crust is unknown. However, we can determine an age range of Late

36    Jurassic to Late Cretaceous from the regional context. We propose a northward-propagating rifting

37    process in the Porcupine Basin, resulting in variations in strain along the rift axis.

38    **1 Introduction**

39    During the rifting of continents, continental lithosphere is stretched until final break-up is reached

40    and an oceanic basin is formed. Magma-poor rifting often results in hyperextension of the

41    continental crust, serpentinization of the mantle beneath the thin embrittled crust [*Boillot et al.*,

42    1989; *O'Reilly et al.*, 1996; *Perez-Gussinye and Reston*, 2001], and unroofing of a broad zone of

43    continental mantle [*Reston*, 2009] before the eventual onset of seafloor spreading.  The rift

44    evolution and key geological processes, such as the distribution of strain during rifting and the

45    syn-rift tectonics, are recorded by the crustal structure and the stratigraphic record and thus best

46    determined by a combination of seismic methods (reflection and refraction) and well data.

47

48    The Porcupine Basin is one of the largest basins in the Irish offshore (Fig. 1), and has a thick Upper

49    Paleozoic to Cenozoic sedimentary infill. The basin currently has a distinct bathymetric

50    expression, reflecting Neogene differential subsidence and under-sedimentation [*Shannon et al.*,

51    2001; *Praeg et al.*, 2005]. Cenozoic subsidence [*Tate et al.*, 1993] increases towards the basin axis

52    and down the axis towards the south, suggesting that crustal thinning might similarly increase and

53    that latitudinal variations in the E-W structure of the basin might reflect different stages of rifting

54    [*Reston et al.*, 2004] from a narrow rift in the north, to a wide, more extended rift and perhaps even

55    a pair of conjugate margins in the south, making it an ideal natural laboratory to investigate rifting

56    processes.

57

58    In this paper, we present newly analysed and interpreted wide-angle seismic data that provide

59    important constraints on the deep structure and the rifting evolution of the southern part of the

60    Porcupine Basin. We use tomographic models of the wide-angle seismic data to define the

61    structure of the crust and upper mantle, while thirteen normal incidence reflection profiles provide

62    information on the sedimentary succession and structure.

63
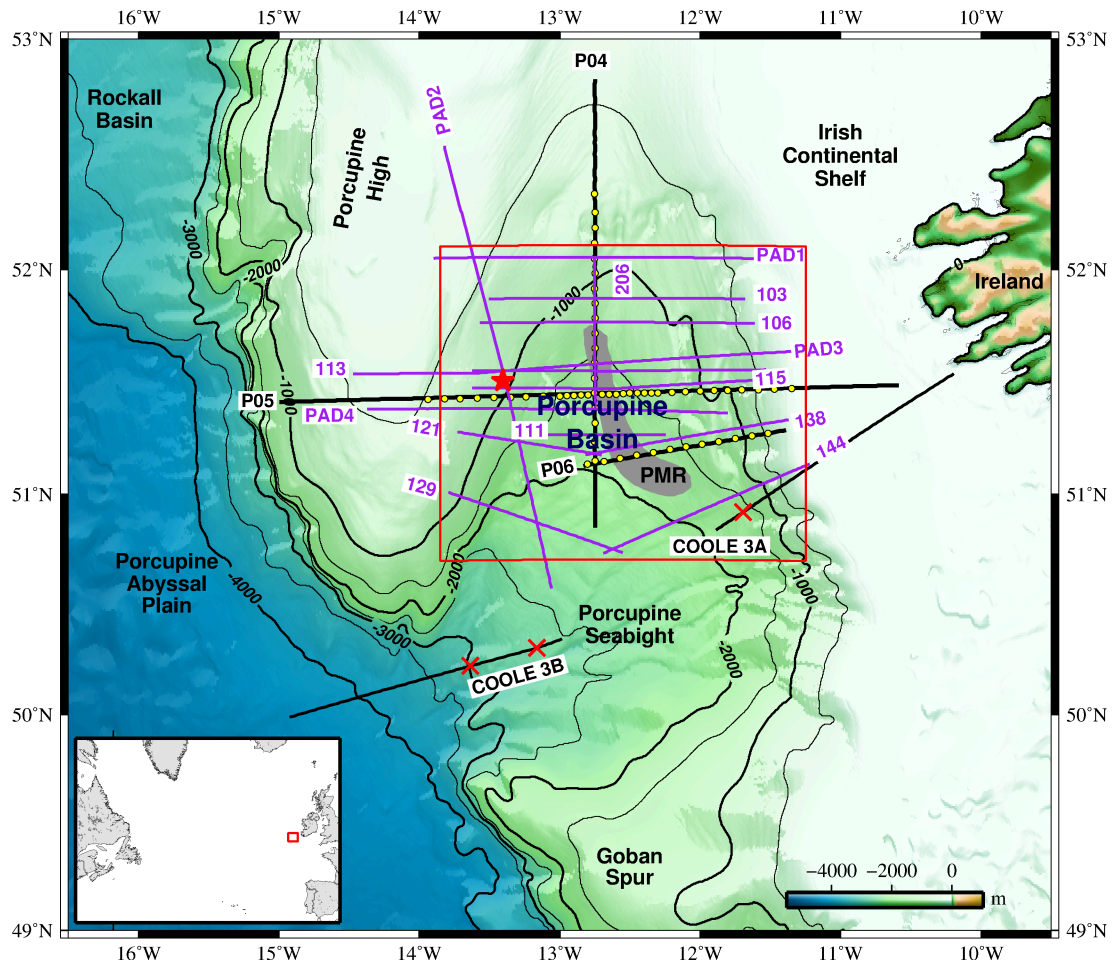


**Fig. 1.** Bathymetric map of offshore Ireland, showing the Porcupine and adjacent basins. Inset shows the location of our study area in North Atlantic. Black lines illustrate the wide-angle shooting profile from M61/2 and COOLE experiment [*Makris et al.*, 1988]. Ocean Bottom Seismometers are illustrated by yellow circles. Red crosses represent the locations of 1-D velocity-depth profiles used in Fig. 9. The red rectangle refers to the location of Fig. 7 and Fig.

3

70    10. Purple lines show the seismic reflection profiles used in this research. Porcupine Median Ridge (PMR) is shown
71    in grey [*Tate, 1993*]. Well 43/13-1 is indicated by the red star.

## 2 Geological Setting

73    The Porcupine Basin is a V-shaped, deep-water sedimentary basin, located in the North Atlantic

74    southwest of Ireland (Fig. 1), between contemporaneous magma-poor continental margins (e.g.

75    Goban Spur [*Bullock and Minshull*, 2005]) in the south, and contemporaneous magma-poor rifts

76    (Rockall Basin) and younger magma-rich continental margins (e.g., Rockall Bank [*Joppen and*

77    *White*, 1990]; Hatton Bank [*Fowler et al.*, 1989]) in the north. The rifted margins north of the

78    Porcupine Basin are influenced by the North Atlantic igneous province [*White et al.*, 2008]. The

79    basin is often considered in several parts: northern and central parts that are both characterized by

80    a N-S trending rift axis, and a southern part, where the rift axis curves towards the SW, before

81    being truncated by Cretaceous oceanic crust of the Porcupine Abyssal Plain [*Naylor et al.*, 2002].

82    For the purposes of distinguishing the changing structure through the Porcupine domain, we

83    consider three regions (northern, central and southern). *Tate* [1993] suggested the main rifting of

84    the Porcupine Basin started near the base of the Bajocian, while *Bulois et al.* [2017] suggested it

85    started in the Upper Jurassic. Nevertheless, the basin's shape and large-scale structure largely

86    reflect significant lithospheric stretching in Mid-Late Jurassic times, with less pronounced rift

87    episodes in the Permo-Triassic and Early Cretaceous [*Shannon*, 1991; *Tate*, 1993].

88

89    Based on subsidence analysis of the Porcupine Basin, *Tate et al.* [1993] estimated that the

90    lithospheric stretching factor increases from less than 1.5 in the north to more than 6 in the south.

91    However, their model lacks constraints from seismic reflection data and well data in the southern

92    Porcupine Basin and does not allow for reduced subsidence resulting from the serpentinization of

93    the uppermost mantle [*O'Reilly et al.*, 1996], to be expected once a stretching factor of ~3 has been

94    reached [*Perez-Gussinye and Reston*, 2001]. Based on the same subsidence data, *Tate* [1993]

95    proposed that the basin formed by clockwise rotation of the Porcupine Bank away from the Irish

96    Mainland and Celtic platforms, leading to a southward increase in stretching factor along the basin

97    axis with a pure-shear stretching mode.

98

99    In the northern part of Porcupine Basin, a high-amplitude, bright and unbroken deep reflector is

100   observed from seismic reflection data, and named the Porcupine Intrabasement Reflection

101    [*Johnson et al.*, 2001] or PIBR [*Reston et al.*, 2001], subsequently shortened to "P" [*Reston et al.*,

102    2004] (Fig. 2a). Based on seismic reflection data, this feature was formally named the Porcupine

103    Arch [*Naylor et al.*, 2002], and  has been interpreted as the top of basement underlying a package

104    of pre-rift sediments [*Johnson et al.*, 2001], or as a detachment fault separating the crust and

105    serpentinized mantle [*Reston et al.*, 2004]. Alternatively, *Gagnevin et al.* [2017] suggest, on the

106    basis of mapping widespread sill complexes in seismic reflection data, that the Porcupine Arch is

107    the top of a large mafic intrusion that fed these sills. Gravity and wide-angle seismic data have

108    been interpreted to suggest that the Arch is the tectonic expression of mantle serpentinization and

109    the consequent formation of detachment faults [*Readman et al.*, 2005; *O'Reilly et al.*, 2006], and

110    that the rifting of this part of the Porcupine Basin is magma-poor. However, its match to the Moho

111    reflector modeled from wide-angle seismic profiles in the northern part of the basin [*Prada et al.*,

112    2017], leads us to favor the feature being the crust-mantle boundary.

113

114    An elongate feature in the deep sediments without an evident gravity anomaly, referred to as the

115    Porcupine Median Ridge (PMR) [*Tate and Dobson*, 1988; *Reston et al.*, 2004], is observed where

116    the Porcupine Arch (or "P") terminates to the south. However, ongoing debate [*Calvès et al.*, 2012]

117    over the structure of the PMR is partly driven by a lack of constraints on the deep structure from

118    available seismic reflection data.  The transition between the Porcupine Arch and the PMR

119    coincides with a sharp change in gravity anomaly, attributed to a NW–SE transfer zone that caused

120    a major change in crustal thickness and tectonic regimes across the structure [*Tate*, 1992; *Readman*

121    *et al.*, 1995; *Readman et al.*, 2005].

122

123    Based on magnetic anomaly data, *Lefort and Max* [1984] considered the crust in the southern part

124    of the Porcupine Basin to be oceanic in character, and suggested limited seafloor spreading in

125    deepest southern basin in mid-Jurassic times (ca. 170 Ma). However, *Masson and Miles* [1986]

126    reinterpreted the same dataset and considered that the amplitudes of the magnetic anomalies (~150

127    nT peak to peak) are too small to be characteristic of oceanic crust. Based on a seismic refraction

128    study along two OBS profiles (COOLE 3A and 3B, location shown in Fig. 1), *Makris et al.* [1988]

129    suggested that highly stretched continental crust is present in the south of the Porcupine Basin. On

130    the basis of gravity and magnetic modelling along a line between the two COOLE profiles, *Conroy*

131  *and Brock* [1989] suggested that the crust is continental in nature, and thins rapidly from the
132  eastern continental shelf to less than 8 km in the center of the basin.

**3 Data acquisition and processing**

134  The seismic reflection data (Fig. 1) discussed in this paper are part of three high quality 2D surveys
135  acquired by Fugro-Geoteam in 1997 (lines 106, 115, 121, 129, 138, 144, 206) and Petroleum
136  Affairs Division (Ireland) in 2013 (PAD2) and 2014 (PAD1, PAD3). Wide-angle seismic data
137  were gathered during F/S Meteor cruise M61/2 in 2004. Here we focus on profiles P04 – P06 (Fig.
138  1), The analysis of P05 was presented by *Watremez et al.* [2016], and the northern part of P04 by
139  *Prada et al.* [2017]; here we analyze data from P06 and the southern part of P04 and integrate
140  results from the three profiles. Both P04 and P06 were acquired with two 32 L Bolt airguns fired
141  at one-minute (~ 130 m) intervals and ocean bottom seismometers (OBSs) spaced at ~8 km.
142  Profiles P04, P05 and P06 are coincident with seismic reflection profiles 206, 115 and 138,
143  respectively (Fig. 1).

144
145  Along the 220-km-long axial profile P04, eighteen ocean bottom seismometers were deployed.
146  Data could be retrieved from sixteen of those instruments. Data quality of profile P04 (Fig. 3a, b)
147  is variable, but in general allowed phase identification out to at least 50-60 km. This makes it
148  possible to identify the reflection (PmP) from the crust-mantle boundary (Moho), as well as the
149  head or diving wave within the uppermost mantle (Pn).

150
151  Twelve ocean bottom instruments were deployed along the 105 km long profile P06 (Fig. 1). The
152  landward receiver gathers are significantly noisier than those located in the center of the basin, as
153  the water depth decreases sharply when approaching the continental shelf. In general, data from
154  all OBSs allowed phase identification out to at least 40 to 50 km (Fig. 3c, d) and thus PmP was
155  identified on most instruments. However, significant delays of the PmP arrival times can be
156  observed compared with those on the northerly instruments (OBS 85 on P04, which is the closest
157  to P05). Pn is not observed on the central instruments because the shooting profile was relatively
158  short.

159
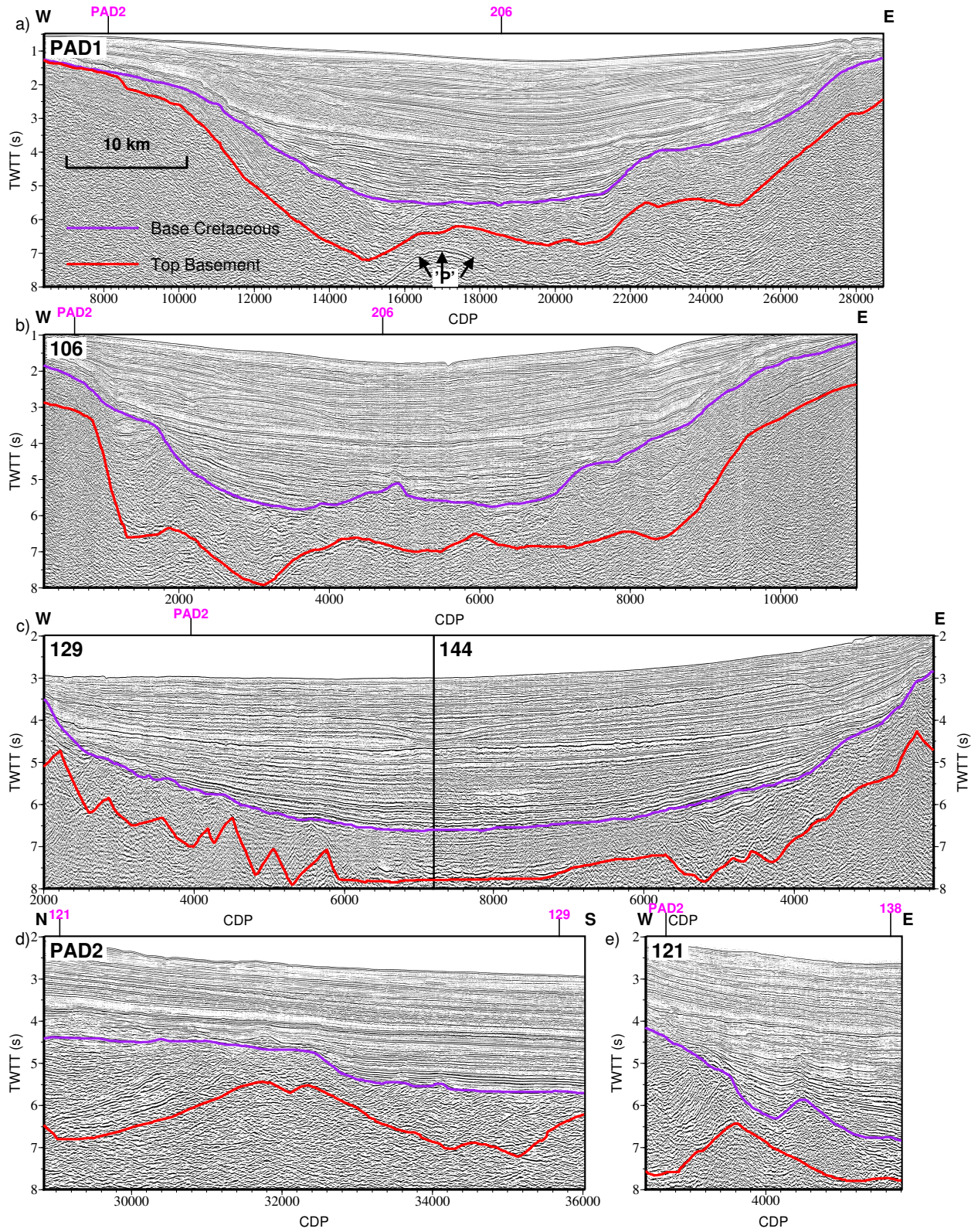
160
161
162  **Fig. 2.** Time-migrated seismic reflection profiles with two major stratigraphic horizons interpreted. The purple
163  horizon corresponds to the Base of Cretaceous. Red line indicates top basement.  The intersection points are marked
164  in pink.

165
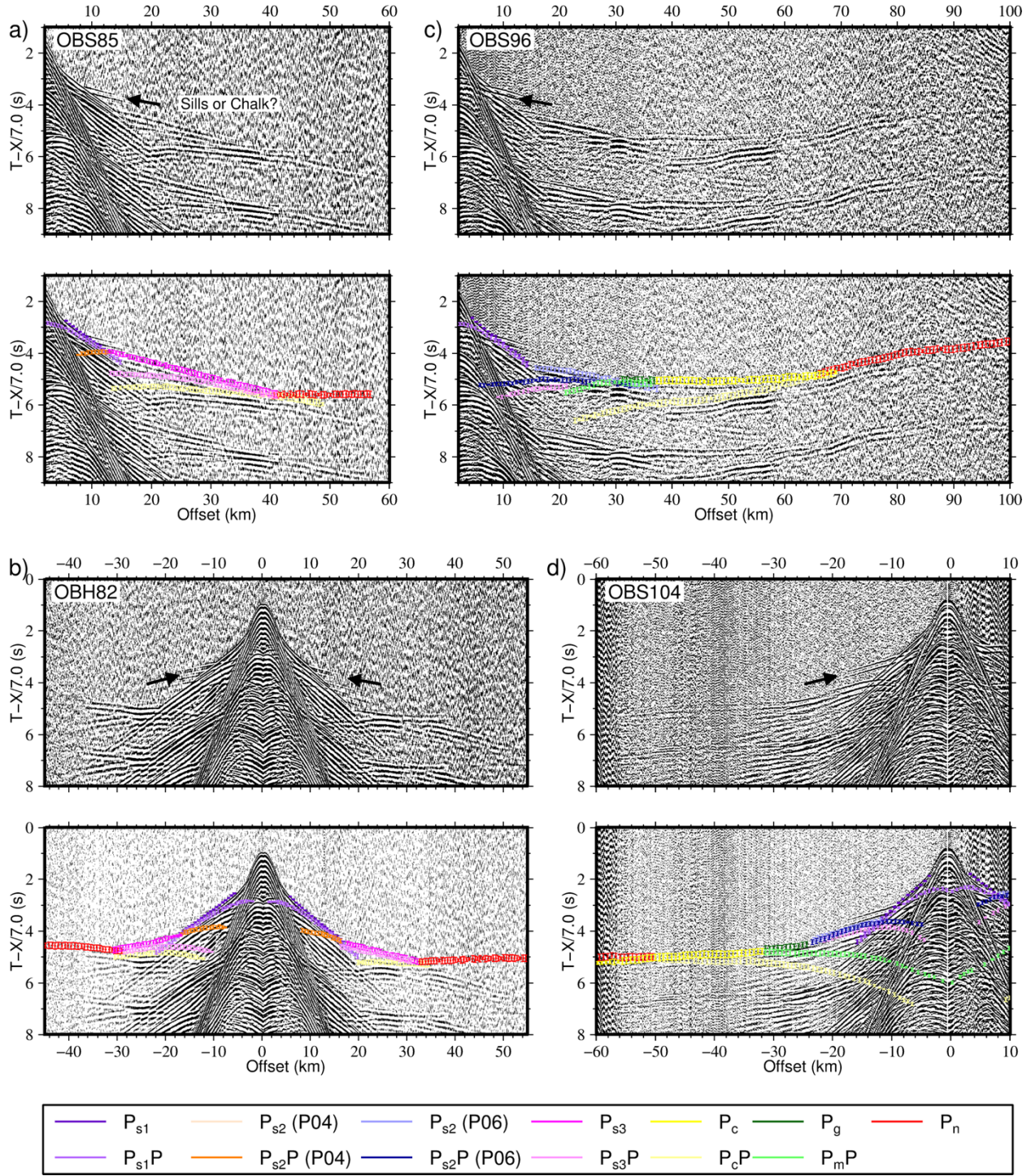


**Fig. 3.** Data and phase picking for instruments 82 and 85 on P04, 96 and 104 on P06. The OBS records are filtered with a 1-3-16-24 Hz bandpass filter for display. Colour bars indicating decimated picks (every five) correspond to different seismic phases, as detailed in the bottom legend. The height of each bar represents its uncertainty. Black arrows indicate the high velocity arrivals from possible sill-complex or chalk.

174   **4 Data analysis**

175   4.1 Phase Identification and Picking

176   A drift correction was applied to the OBS clocks, as clock drift can be a source of significant error.

177   The P-wave arrivals were picked manually on unprocessed seismic records at short offsets, and on

178   filtered data for far-offset arrivals. In order to improve the signal-to-noise ratio at far offsets, a

179   minimum phase Butterworth bandpass filter (1-3-16-24 Hz) was applied.  Both the hydrophone

180   and vertical geophone were used to identify the best quality arrivals, and then used accordingly for

181   the phase picking. Picking uncertainties were estimated using the signal to noise ratio of the traces

182   within ± 250 ms of the picked arrivals, using the empirical relationship as in *Zelt and Forsyth*

183   [1994] and an offset dependent relationship for offsets < 40 km. The assigned picking uncertainties

184   vary from 20 to 125 ms (Fig. 3).

185

186   Along P04, phase identification is difficult due to changes from north to south in the seismic

187   structure of both the sedimentary succession and the basement. In total, two sedimentary phases

188   (Fig. 3a, b) were identified, with apparent velocities of 1.60 – 3.5 km/s and 3.75 – 5.25 km/s. The

189   PmP Moho reflection phase was identified, but no refractions within the crust could be picked.

190   On profile P06, a sedimentary seismic phase (Fig. 3c, d) with an apparent velocity 3.15 km/s was

191   identified along the entire line. Beneath this, a higher velocity phase with an apparent velocity 4.6

192   - 5.1 km/s was observed on almost all the instruments on the line, also on some of the instruments

193   along P04 and P05. By converting the zero-offset reflection time of this phase into two-way travel

194   time, we infer that it corresponds to the top of the Upper Cretaceous Chalk layer interpreted from

195   the seismic reflection data [*Shannon et al.*, 2007]. Upper Cretaceous Chalk has been drilled by

196   well 43/13-1 (Fig. 1) underlying basalts on the western flank of the Porcupine Basin [*Baxter et al.*,

197   2001; *King*, 2016]. This phase is most likely generated either by the Chalk itself or by the Chalk

198   together with an overlaying igneous lava/sill complex. This phase was not used in our tomographic

199   modeling because the associated smoothing deals poorly with velocity inversions. As a shadow

200   zone was created below the high-velocity phase, only one complete pair of refracted and reflected

201   sedimentary phases could be identified, which travelled inside PMR on several western

202   instruments on P06. An additional sedimentary layer below was identified only from reflections

203   on a few instruments (e.g. OBS96, 104). The corresponding refractions are difficult to distinguish

204    from those from the basement below, perhaps due to very similar velocities and the reduced

205    thickness of this layer. Two basement layers and the upper mantle were identified with apparent

206    velocities of 5.8 - 6.3 km/s, 6.6 - 7.2 km/s and 7.5 - 8 km/s, respectively.

207    4.2 Modelling Strategy

208    Prior to tomographic analysis, a forward modeling exercise using the code of *Zelt and Smith* [1992]

209    was carried out to ensure correct phase identification. Picked travel times from profiles P04 and

210    P06 were modeled using TOMO2D [*Korenaga et al.*, 2000], following the approach previously

211    applied to P05 [*Watremez et al.*, 2016]. This tomography method uses a hybrid approach based on

212    the graph [*Moser*, 1991] and ray bending methods [*Moser et al.*, 1992] to calculate the travel time

213    residuals by forward ray-tracing through a given starting model, and then solves a linearized

214    inverse problem using a least-squares algorithm [*Paige and Saunders*, 1982] to reduce the

215    residuals iteratively. In order to retrieve the P-wave velocity structure and the geometry of

216    reflectors with a high resolution, a joint refraction and reflection travel time inversion was

217    performed following a top-down layer-stripping approach [*Sallarès et al.*, 2013]. This approach

218    allows the model to contain sharp discontinuities and avoids building an entirely smooth model.

219    The model was built, layer by layer, resolving the velocity and interface structure of each layer at

220    different steps. For each step, the starting velocity models were defined carefully based on the

221    apparent velocities observed for the given phase, together with the velocities retrieved from the

222    previous layer.

223    **Table 1**. Modelling statistics for all the layers built for P04 and P06. $t_{RMS}$ is root-mean-squared travel-time residual;
224    $\chi 2$ is normalised chi-squared. $6^{Ref}$ represents the step to invert the separate floating reflector (pink interface in Fig. 4c)
225    with all the refractions together.

226

| Line | Step | Number of refractions | Number of reflections | $t_{RMS}$(ms) *refractions* | $t_{RMS}$(ms) *reflections* | $t_{RMS}$ (ms) *all* | $\chi^2$ refractions | $\chi^2$ reflections | $\chi^2$ all |
|---|---|---|---|---|---|---|---|---|---|
| P04 | 1 | 4634 | 5159 | 14 | 30 | 24 | 0.19 | 0.41 | 0.30 |
| P04 | 2 | 5252 | 2676 | 20 | 52 | 34 | 0.19 | 0.83 | 0.41 |
| P04 | 3 | 8979 | 4658 | 38 | 67 | 50 | 0.29 | 0.81 | 0.47 |
| P04 | 4 | 8979 | 5241 | 33 | 50 | 40 | 0.23 | 0.39 | 0.29 |
| P04 | 5 | 16467 | 5241 | 63 | 49 | 60 | 0.45 | 0.39 | 0.44 |
| P06 | 1 | 2067 | 1978 | 23.51 | 31.62 | 27.77 | 0.93 | 0.57 | 0.75 |
| P06 | 2 | 3452 | 2496 | 45.17 | 40.06 | 43.10 | 1.64 | 0.57 | 1.18 |
| P06 | 3 | 4313 | 3262 | 45.32 | 94.75 | 70.96 | 0.46 | 0.95 | 0.97 |
| P06 | 4 | 6681 | 4527 | 48.53 | 76.75 | 61.51 | 0.43 | 0.92 | 0.63 |
| P06 | 5 | 8121 | 4527 | 51.90 | 77.32 | 62.21 | 0.50 | 0.89 | 0.64 |
| P06 | $6^{Ref}$ | 8121 | 874 | 115.44 | 125.63 | 116.44 | 2.85 | 6.29 | 3.18 |

227

228
229
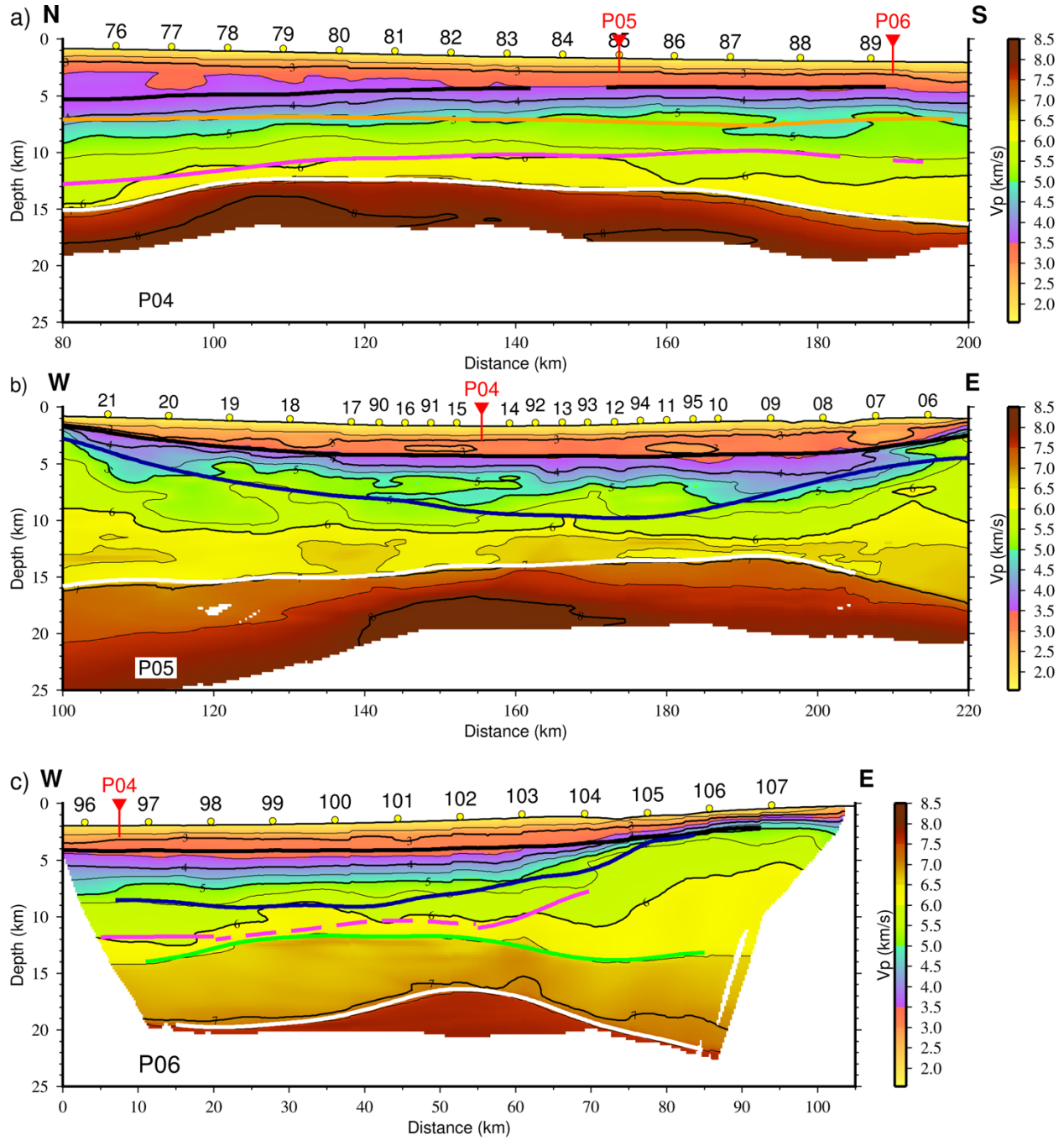


**Fig. 4.** Final velocity models for profile P04 (a), P05 (b) and P06 (c). Colored lines show the interfaces modelled for different layers. Black marks the interpreted base Tertiary; orange marks the interpreted base Albian; blue marks the interpreted base Cretaceous; pink marks the interpreted top of basements (dashed where no reflected phases were observed and modelled); Green illustrates the interface within the crust and white is the Moho. Red triangles mark the intersection points where the profiles cross each other. Plots have a vertical exaggeration of 1.5.

Grid spacing for the models was 0.25 x 0.25 km. The velocity model of profile P04 (Fig. 4a) was

built in five steps, and has six layers. For P06, the model had five layers and one floating reflector

239    for the top of basement, built via six steps. Travel time picks and misfit statistics for the final

240    velocity models of P04 and P06 are detailed in Table 1. Travel time misfits and the chi-squared

241    statistics for each individual layer are mostly less than 100 ms and 1.0, respectively.

242

243    4.3 Resolution and Uncertainty

244    4.3.1 Derivative weight sum

245    Ray coverage through the final velocity models of P04 and P06 (Fig. 5a, e) is represented by the

246    derivative weight sum (DWS), which is a weighted measure of the total ray length through each

247    node in the inversion grid. The models are better resolved where a high DWS is achieved, while

248    low DWS values are associated with regions of poor ray coverage that are not resolved and should

249    not be interpreted. The ray coverage along P04 (Fig. 5a) is best between model distances 80 and

250    180 km, down to 16 km depth. This is the area where ray coverage is the densest and rays are

251    travelling in both directions. Excellent ray coverage was achieved oceanwards along P06 (Fig. 5e)

252    from model distance 20 to 60 km. Good ray coverage was observed basin-wide up to the Moho

253    depth where we had instrument coverage. Ray coverage was moderate to poor under the

254    continental shelf, where many of the velocity cells are only sampled by unidirectional ray paths.

255    4.3.2 Monte Carlo uncertainty analysis

256    The Monte Carlo uncertainty test [*Korenaga et al.*, 2000] was used to assess quantitatively the

257    uncertainty associated with the final velocity model. This test evaluates the variability of

258    acceptable solutions for a range of starting models and a range of possible travel-time picks, for a

259    given set of smoothing and inversion parameters (e.g. [*Korenaga and Sager*, 2012]) and hence is

260    a good measure of relative uncertainty but a poorer measure of absolute uncertainty. For both the

261    profiles, 100 model realizations and tomographic inversions were performed for each layer using

262    the same parameters which generated the final velocity models in Fig. 4, by creating 100

263    corresponding randomized input velocity models, randomized reflector depths, and randomized

264    travel-time datasets with Gaussian noise. These travel-time datasets were generated by adding

265    randomized timing errors, including a common receiver error (± half the maximum receiver error,

266    ± 62.5 ms), and  picking errors.

267

268    The parameter ranges used in the starting model for P04 and P06 are listed in Table 2. The average

269    velocity model of P04 (Fig. 5b) is very close to the best-fitting model (Fig. 4a), with sediments

270    thickening toward the north, and similar Moho geometry. The velocity standard deviations (Fig.

271    5c) are generally lower than 0.1 km/s. However, the uncertainties are higher at the southern end of

272    the model because the ray coverage is sparser and unidirectional. In the crust, the uncertainties are

273    slightly higher than 0.1 km/s where no refractions were picked because of a combination of a thin

274    crustal layer and high mantle velocities.

275

| Line | Step | $V_P$ top (km/s) | $V_P$ bottom (km/s) | Interface depth (km) | |
| --- | --- | --- | --- | --- | --- |
| | | | | North | South |
| P04 | 1 | 1.8 ± 0.05 | 4.0 ± 0.2 | 5 ± 0.5 | 4 ± 0.5 |
| P04 | 2 | 3.5 ± 0.2 | 5.0 ± 0.3 | 7.5 ± 1 | 7.5 ± 1 |
| P04 | 3 | 4.8 ± 0.2 | 6.0 ± 0.5 | 10 ± 2 | 10 ± 2 |
| P04 | 4 | 6.0 ± 0.4 | 7.0 ± 0.3 | 25 ± 5 | 20 ± 5 |
| P04 | 5 | 7.5 ± 0.4 | 8.0 ± 0.1 | 28.5 ± 2.5 | 28.5 ± 2.5 |
| P06 | 1 | 2.5 ± 0.125 | 3.0 ± 0.15 | 5 ± 1 | |
| P06 | 2 | 3.5 ± 0.175 | 5.5 ± 0.275 | 10 ± 1 | |
| P06 | 3 | 5.7 ± 0.285 | 6.2 ± 0.31 | 14 ± 2 | |
| P06 | 4 | 6.7 ± 0.67 | 7.1 ± 0.71 | 18 ± 2 | |
| P06 | 5 | 7.5 ± 0.75 | 8.1 ± 0.81 | 18 ± 2 | |

276    **Table 2**. Ranges of values used for the model parameterization of P04 in the Monte-Carlo analysis.

277

278    Along P06, the average velocity model (Fig. 5f) of P06 is very close to the best-fitting model (Fig.

279    4c). The crust beneath the continental shelf exhibits velocity uncertainties of ~ ± 0.1 km/s from 75

280    to 90 km, which are related to insufficient ray coverage. At 25 - 35 km of profile distance, the

281    higher velocity zone observed from depth 7 to 9 km on the model (Fig. 4c), which corresponds to

282    the location of the PMR shows uncertainty of ~ ± 0.1 km/s. Two lobes of high uncertainties ~ ±

283    0.1 km/s appear in the upper layer of crust due to the sharp geometry adapted from the upper

284    reflector in the starting model.

285    4.3.3 Resolution Test

286    We performed a series of checkboard test of model resolution to estimate the lateral resolvability

287    of the models [*Zelt*, 1998]. This allowed us to estimate the smallest feature that can be resolved

288    for each model cell. For both profiles, we perturbed the final tomographic model with a cell of 5%

289    positive and negative velocity anomalies, and traced and calculated synthetic arrival times

290    corresponding to our picks. These travel times were then perturbed with random noise as in the

291    Monto Carlo test, and inverted together with the final model. For each square cell size (increasing

every 2 km from 2 to 20 km), we tested in total of eight checkboard patterns, including opposite

polarity for the cell, 45°rotation of the cell, and cells shifted by half of the cell size vertically and

horizontally to remove the effects of polarity and registration.
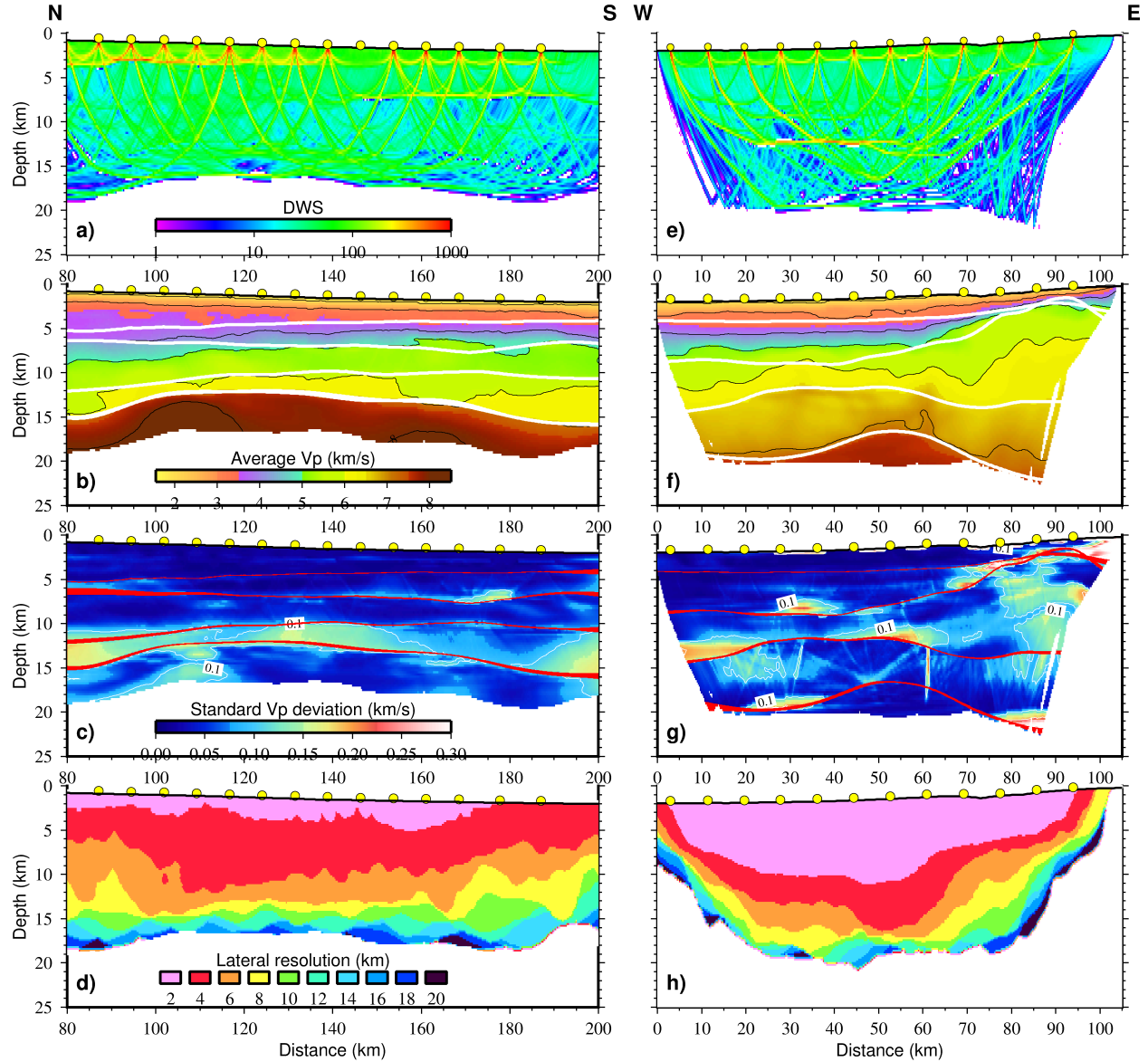


**Fig. 5.** Derivative weight sum of seismic rays traced through the velocity model of P04 (a) and P06 (e). Higher DWS values indicate areas with a higher density of sampled rays. (b) and (f) are the mean P04 and P06 velocity models from the Monte Carlo uncertainty test. White lines illustrate the average interfaces from all the model realizations for each layer. (c) and (g) show the standard deviations of velocity models derived from all the starting models for each layer, with the thickness of the red lines marking the standard deviations of interface depth. (d) and (h) show the lateral velocity resolution for P04 and P06 from 80 checkboard tests. Coloured regions represent the minimum cell sizes can be resolved by the model. White regions have lateral resolution larger than 20 km or are unsampled. Plots have a vertical exaggeration of 2.0.
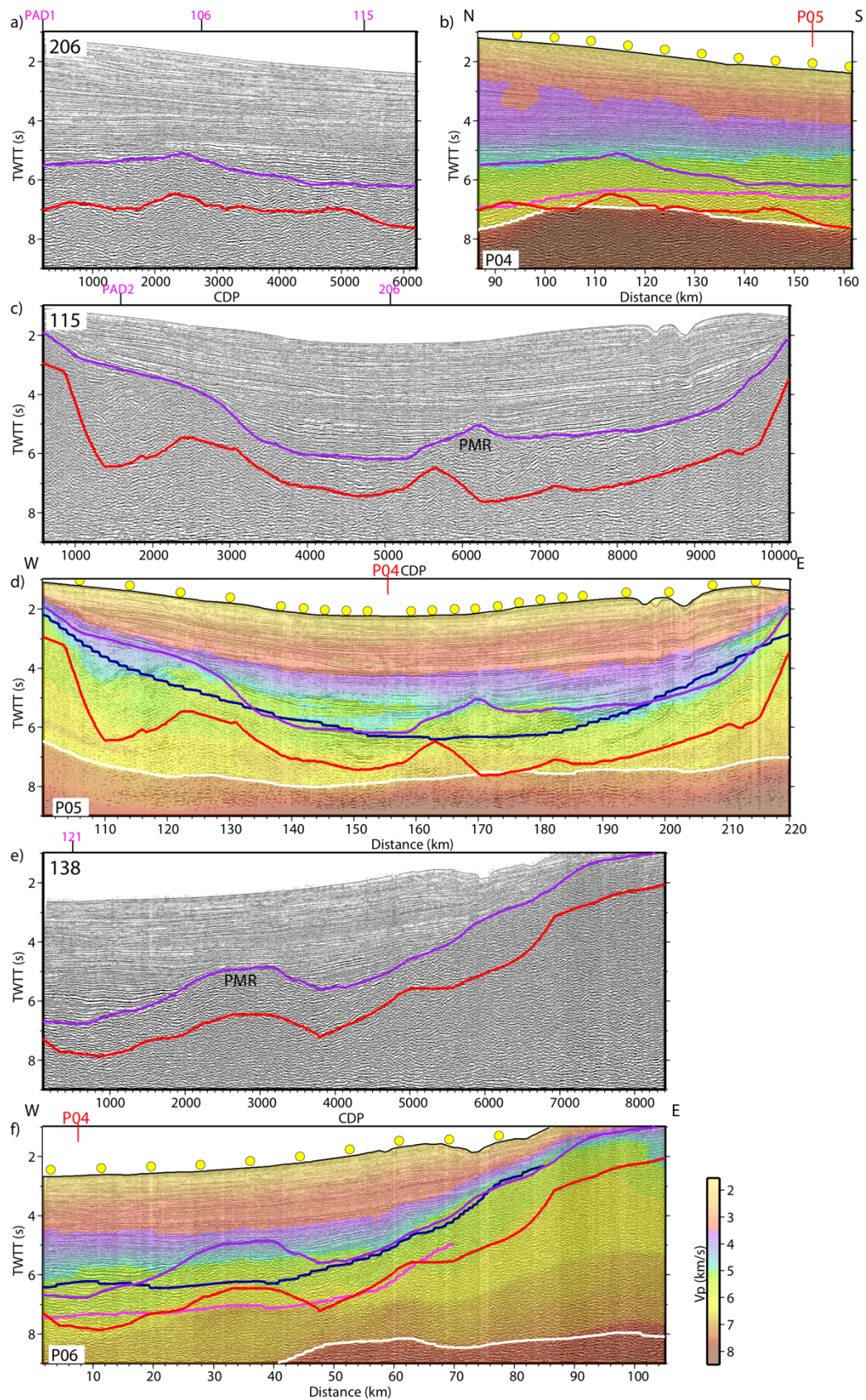
305

306   Fig. 6. Comparison between velocity models and coincident seismic reflection records. Purple and red lines are the
307   same as in Fig. 2. The other colored lines are the same as in Fig. 4. (a) Time-migrated seismic reflection record 206.
308   (b) Overlay of the time-converted velocity model P04 on coincident seismic reflection profile 206. (c) Time-migrated
309   seismic reflection record 115, which is coincident with P05. (d) Overlay of the time-converted velocity model P05 on
310   115. (e) Time-migrated seismic reflection record 138, which is coincident with P06. (f) Overlay of the time-converted
311   velocity model P06 on 138.

312

313   The semblance (resolvability) was then calculated between the input and output patterns within a

314   5 km operator radius. The checkerboard pattern is considered to be well resolved if the semblance

315   >= 0.7 [*Zelt*, 1998]. The semblance grids for each cell size are then averaged and interpolated to

316   show the minimum cell size can be resolved at each velocity node.

317
318   A good resolution of 4 km along P04 is obtained between model distances 100 and 170 km, down

319   to 8 km depth (Fig. 5d). Thus, the structure sizes that can be resolved then increase gradually with

320   depth. A structure size of at least 2 km (smallest perturbation pattern) is resolved in the central

321   basin along P06, down to 10 km depth (Fig. 5h). Slightly larger structures with a size of 4 km can

322   be resolved at 13 km depth on the basin flank and up to 17 km depth from 40 to 60 km along the

323   model. Generally, the resolution within the basement allows us to interpret structures on a length

324   scale of 6 km and for the lower basement layer, 8 km.

325   4.4 Seismic Reflection Data

326   In order to gain further constraints on the crustal structure and the tectono-sedimentary evolution

327   of the basin, the distribution of sediments and two-way travel time (TWTT) to top of basement

328   were mapped on time-migrated seismic reflection data by tracing the stratigraphy away from well

329   43/13-1 (Fig. 1), and also taking into account previous interpretations of individual or multiple

330   profiles [*Moore and Shannon*, 1995; *Baxter et al.*, 2001; *Johnson et al.*, 2001; *McDonnell and*

331   *Shannon*, 2001; *Naylor et al.*, 2002; *Reston et al.*, 2004; *Calvès et al.*, 2012].

332

333   Seismic reflection data used in this study are generally of very good quality and reveal a wealth of

334   seismic stratigraphic information (Fig. 2, 6), especially in the Cenozoic to Cretaceous successions

335   [*Shannon et al.*, 2007]. The Base Cretaceous unconformity that we picked is characterized by a

336   well-defined strong reflective event that appears to separate the interpreted post-rift and syn-rift

337   sections, and deepens from the continental shelf to the central basin. However, these data generally

338   fail to clearly image the top of basement and the Moho, so could not be used to constrain these

339     boundaries in our velocity models. In addition, the lack of deep borehole information in the basin

340     makes it difficult to identify a precise reflector corresponding to the top of the basement. We

341     picked a horizon that maps the bottom of titled fault blocks, above which the sediments exhibit

342     clearly layered features.  We are confident that basement rocks are not present above this horizon,

343     but cannot exclude the possibility that poorly imaged sediments are present beneath it.



344
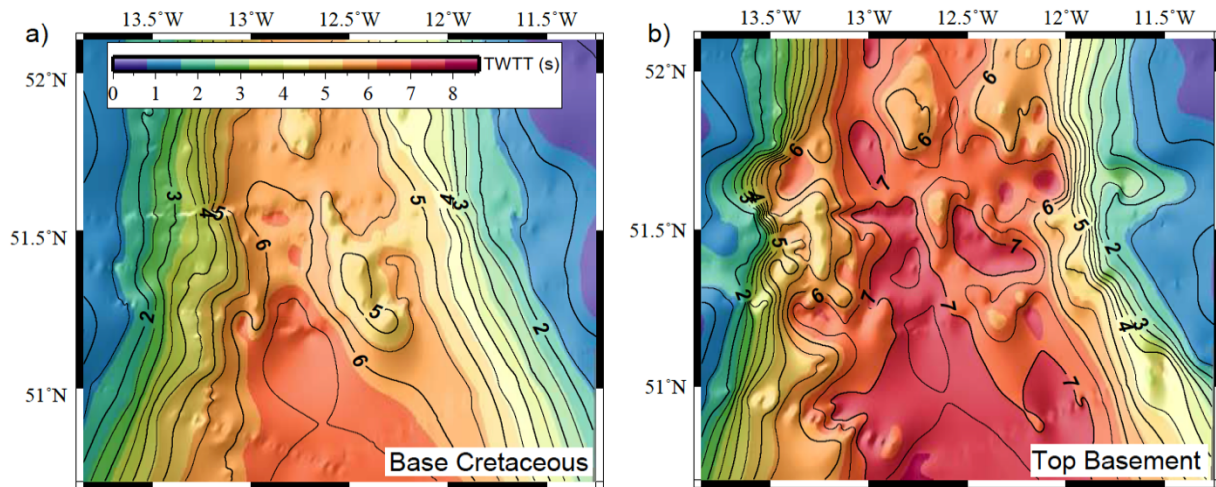
345 **Fig. 7.** Isochron maps of interpreted stratigraphic horizons. (a) Base Cretaceous unconformity. (b) The top of
346 basement.
347

348     We have compared these horizons with the reflectors modeled from the OBS data (Fig. 6). The

349     Base Cretaceous interface (blue line in Fig. 6d, f) inferred from wide-angle data corresponds in

350     general to the Base Cretaceous horizons (purple lines in Fig. 6c, d, e, f) picked on the reflection

351     data. The variation of the Base Cretaceous unconformity along P04 makes the OBS modelling of

352     this interface quite difficult, so a more consistent horizon above the Base Cretaceous was modeled

353     (orange reflector in Fig. 4a), which corresponds to the Base Albian horizon.  Beneath the Base

354     Cretaceous unconformity, pre-Cretaceous sediments with a maximum velocity of 5.8 km/s were

355     observed at the southern end of P04 and both sides of the PMR on P06.  A perfect match was not

356     achieved between horizons inferred from wide-angle and normal incidence data because the OBS

357     data become more complex with increasing depth, and normal incidence reflections become more

358     difficult to pick.

359

360  On thirteen seismic reflection profiles, we interpret  a post-rift sedimentary unconformity (Base

361  Cretaceous), and the top basement (Fig. 2, 6). These two horizons were then interpolated into

362  isochron maps (Fig. 7).

363
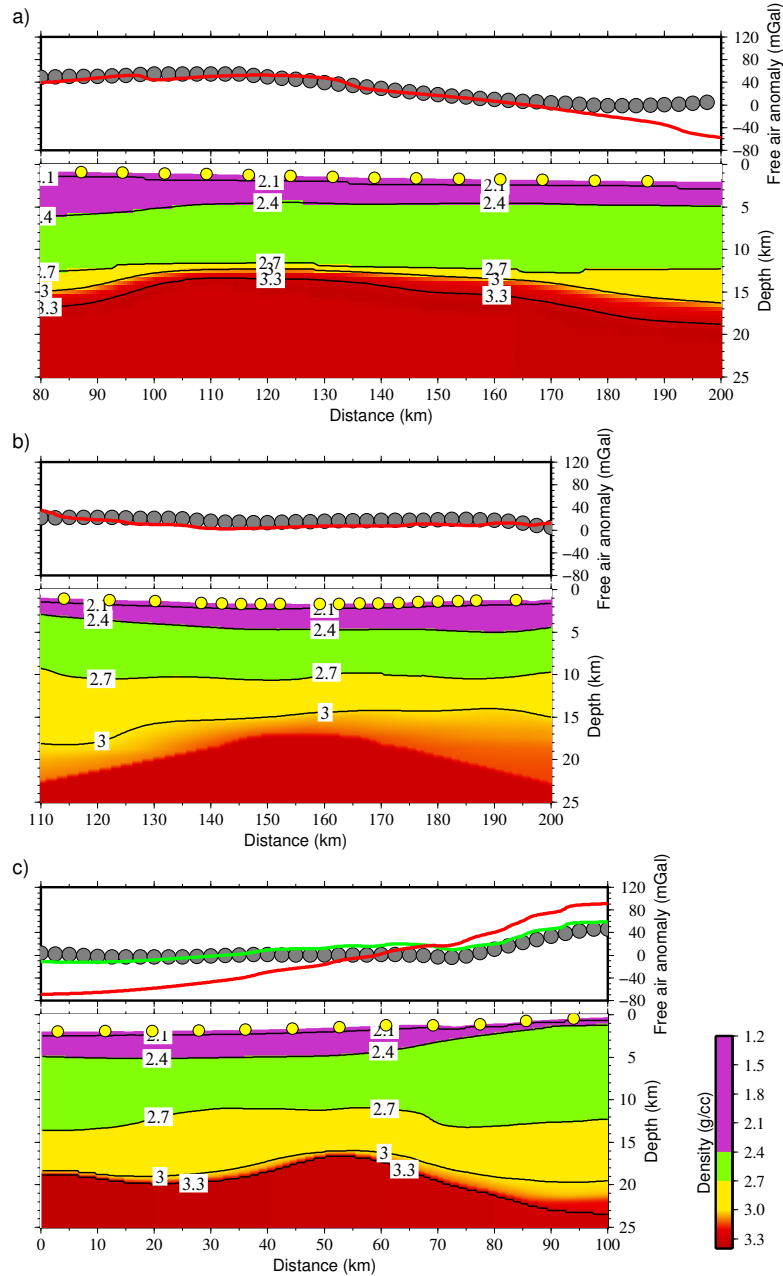


364
365  **Fig. 8.** Free air gravity modelling results for P04 (a), P05 (b) and P06 (c). Upper panel: grey circles mark the
366  observed (free air gravity anomaly. The red line represents the calculated gravity anomaly from the density models
367  below derived from the velocity-density relationships. The green line in c) represents the calculated gravity anomaly
368  from a model with mantle density variations described in the text. Models were extended 500 km from each edge to
369  avoid edge effects. Lower panel: Density model derived from the corresponding seismic velocity model.

370  **5 Results**

371  5.1 Velocity Models

372  The final velocity models show many distinct features including: the geometry of the crystalline

373  basement and the PMR, the thinning of the crust, and the velocities in the upper mantle. The P04

374  model (Fig. 4a) shows that the velocity of the sedimentary layers increases southward as the

375  basement deepens, perhaps due to compaction. Lateral variations in the crustal velocities and

376  thickness are also observed along P04. The crust thins from the north and is thinnest at around 100

377  km. From 100 to 160 km, the crust has a velocity of 6.0 - 7.5 km/s and a thickness of $2 - 3.5$ km.

378  From 160 to 200 km, Moho depth increases significantly from 14 to 18 km. However, the model

379  is less constrained towards its southern end, where there are no more OBS and all the rays are

380  unidirectional.

381

382  The P05 model (Fig. 4b) shows that velocities beneath the PMR increase rapidly from 5.5 to 7.0

383  km/s in the center of the basin from 140 to 160 km, and increase from 7.5 to 8 km/s within 2 km

384  below the modelled Moho reflector [*Watremez et al.*, 2016]. P06 (Fig. 4c) shows the velocity

385  structure of the southern Porcupine basin. The uppermost sedimentary layer has velocities of 1.7 -

386  3.4 km/s, matching the upper sedimentary layer observed in profile P04 and P05. In the second

387  layer, velocity ranges from 3.5 to 5.5 km/s. The PMR is located at 20 to 40 km within this layer,

388  and exhibits slightly higher velocity. The distinctive third interface (pink line in Fig.4c) indicates

389  the presence of a high-velocity sedimentary layer. Velocities in the upper basement layer,

390  interpreted as upper crust, range from 5.8 to 6.5 km/s. Velocities in the lower basement layer,

391  interpreted as lower crust, increase from 6.5 km/s to 7.2 km/s at the Moho, with upper mantle

392  velocities beneath the Moho being ~ 7.8 km/s. The thickness of the crust varies from ~7 km in the

393  center of the basin (~15 km) to ~8 km at 30 km (beneath the PMR), and ~5.5 km beneath the

394  eastern flank of the basin (~ 50 km). The crustal velocity (5.0 – 7.1 km/s) beneath the continental

395  shelf (> 75 km) is close to continental velocities observed onshore Ireland [*Hauser et al.*, 2008].

396      5.2 Seismic Reflection Data

397  The Base Cretaceous unconformity (Fig. 7a) is relatively flat in the basin, and deepens steeply in

398  TWTT towards the south as the water depth increases,, while the structural high between 51$^{\circ}$N and

399  51.6$^{\circ}$N maps the top of PMR. The basin can be divided into distinct zones from north to south

400 based on the reflection characteristics of the upper basement and the lateral coherence of the top

401 basement reflector (Fig. 7b). Between reflection profiles PAD1 and 106, where the Porcupine Arch

402 (or "P") is imaged (e.g. from 6.8 – 8 s TWTT along CDP 15400 - 19000 in Fig. 2a), a series of

403 rift-associated tilted fault-blocks are observed, along with steeply-dipping border faults extending

404 into lower crust and connecting with the Porcupine Arch.

405

406 For the profiles located in the southern Porcupine Basin where the Porcupine Arch (or "P") is

407 absent, the MCS data available for the present paper are not able to image the Moho. From profile

408 113 to PAD3, the PMR is observed with a prominent high-amplitude seismic event marking its

409 top, and a low-amplitude reflector for the bottom, whereas chaotic reflections dominate the center.

410 In addition, less large-scale faulting and fewer titled fault blocks are observed in the central basin

411 in this area.

412

413 A significant change in the basement morphology is observed further south. On profile 138 (Fig.

414 6e), from CDP 2000 to 4000, the basement shows a rough, hummocky surface coincident with the

415 PMR, below which no coherent reflections can be seen. The rough basement morphology

416 terminates at CDP 2000 and a smooth continuous reflector caps the basement to the west before

417 another (possibly volcanic) ridge is seen to disrupt the basement at CDP 5000 on reflection profile

418 121 (Fig. 2e). Furthermore, the central basin lacks identifiable pre-rift sediments. Further south, a

419 relatively continuous and undisturbed top basement is observed in the middle of basin (Fig. 2c),

420 where no pre-rift sediments were identified.

421 5.3 Velocity-Derived Density models

422 A comparison between satellite free-air gravity anomaly and the anomaly calculated for density

423 models derived from the velocity structures (Fig. 8) can provide further information on the crustal

424 lithology. The final velocity models (Fig. 4) were complemented with gravity modelling in

425 different ways. First, the free air gravity anomaly was calculated using the method of *Korenaga et*

426 *al.* [2001], by converting the seismic velocities into densities using different empirical velocity-

427 density relationships for different geological layers, to generate a vertically and laterally

428 heterogeneous 2D density model. For the sediments, *Hamilton's* [1978] empirical relation for shale

429 was used. For the unaltered mantle (>= 8 km/s), density was fixed at 3300 kg/m$^3$. Elsewhere,

430    *Carlson and Miller's* [2003] conversion law for low temperature serpentinized peridotite was
431    applied (Fig. 8a, b, c).

432

433    The calculated gravity anomaly for P04 (Fig. 8a) fits the observed anomaly very well at < 160 km.
434    However, an increasing misfit is observed to the south, reaching a maximum 70 mGal. A misfit of
435    the same amplitude occurs on the western side of P06 (Fig. 8c), despite the fact that P06 is oblique
436    to the opening direction. The calculated gravity anomaly fits well with the satellite anomaly for
437    P05 (Fig. 8b).

438

439    The misfits indicate that the adopted velocity-density conversion using a uniform relationship for
440    the whole profile, and attribution of all of the gravity anomaly to density variations in the depth
441    range of the velocity models, are probably over-simplifications. To address these issues, we added
442    to P06 variations in mantle density that could be attributed, for example, to variability in melt
443    depletion or temperature. Assuming that the average lithospheric thickness is 100 km [*Fullea et*
444    *al., 2014*], the lithospheric mantle density at the western end of P06 was set at 3350 kg/m$^3$ and
445    decreased gradually to 3300 kg/m$^3$ beneath the continental shelf. The fit to the observed data was
446    then improved. The fit for P04 and P06 can be further improved by the insertion of high density
447    blocks (3000 kg/m$^3$) at >160 km on P04 and <60 km on P06 to replace the original crustal densities.

448    **6 Discussion**

449    In order to gain insights into the nature of the crust, we compare one-dimensional velocity-depth
450    profiles (Fig. 9) through the three velocity models. Interpretations derived from the P-wave
451    velocity and density models are discussed jointly in this section in addition to features observed
452    on seismic reflection data, gravity data (Fig.10a) and the interpreted top of basement. Three distinct
453    zones (Fig.10b) characterized by different crustal types can be defined in the Porcupine Basin on
454    the basis of their velocities and seismic reflection characteristics.

455    6.1 Southern Porcupine Basin

456    6.1.1 Nature of the crust

457    Oceanic crust and highly stretched continental crust are both bounded downwards by a sharp jump
458    to ~8 km/s (the Moho) and can have similar thickness and seismic velocities, but can be

459    distinguished by their velocity gradients. High velocity gradients in the top ~ 2 km underlain by

460    low velocity gradients (~ 0.1 - 0.2 /s) and a high velocity down to a Moho at ~ 6 - 7 km are typical

461    of oceanic crust [*Spudich and Orcutt*, 1980]; although heavily intruded continental crust may

462    exhibit similar lower crustal velocities, the crust is generally much thicker [*Joppen and White*,

463    1990]. Where not so intruded, thin, stretched continental lower crust generally has a lower velocity

464    (partly as a result of intense deformation and fracturing) than similar thickness oceanic crust,

465    perhaps with a much lower velocity gradient (< 0.1 /s) [*Christensen*, 1995]. Exhumed mantle in

466    contrast typically has a high velocity gradient (~ 1 /s) representing downward decreasing amounts

467    of serpentinization until unaltered mantle velocities of ~ 8 km/s are reached, with a less abrupt

468    Moho [*Minshull*, 2009]. Using these criteria, we can distinguish basement types along the profiles.

469
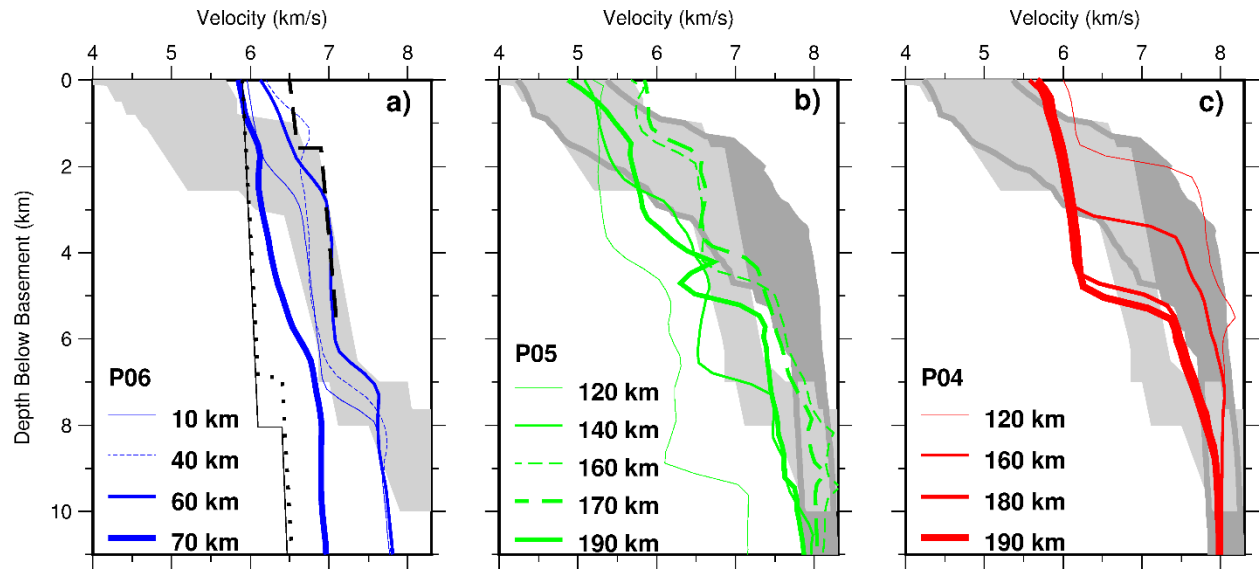


**Fig. 9.** 1-D velocity-depth profiles through the three final velocity models. Depths are measured from the top of the crust in the velocity models (see text). (a) Blue lines represent the 1-D velocity-depth profiles of P06 at different model distances, as shown in the figure. Dashed blue line indicates velocity-depth profiles beneath the PMR. The Light grey shading indicates the velocity envelope for Atlantic oceanic crust aged 59 -170 Ma [*White et al.*, 1992]. Dashed and dotted black line represent the velocity-depth profiles extracted from the western and eastern red cross (Fig. 1) of COOLE 3B [*Makris et al.*, 1988], respectively. Thin black line illustrates the velocity-depth profile from COOLE 3A [*Makris et al.*, 1988](b) Green lines represent the velocity-depth profiles of P05 at different model distances, as shown in the figure. Dashed green lines indicate velocity-depth profiles beneath the PMR. The dark grey shading illustrates the velocity compilation from COT by *Minshull* [2009]. However, as top basement is not modeled by Watremez et. al [2016], the closest reflector (blue line in Fig. 4b) is taken to calculate the depth. (c) Red lines represent the velocity-depth profiles of P04 at different model distances, as shown in the figure.

484    The thin high-velocity crust west of 60 km model distance on P06 (Fig. 9a) is unlikely to be

485    continental. On both sides of the PMR (< 20 km, > 40 km), the upper 2 - 2.8 km of the basement

486    has an average velocity gradient of 0.27 /s, and velocities ranging from 5.8 – 6.6 km/s. Beneath

487     this, velocities increase smoothly to 7 - 7.1 km/s over the next 4 - 4.5 km, with a ~0.125 /s gradient,

488     before increasing sharply to 7.8 - 8.0 km/s in the uppermost mantle.  The velocity-depth profiles

489     at 10 and 60 km (Fig. 9a) thus lie mainly within the envelope of normal oceanic crust [*White et*

490     *al.*, 1992]. In between (40 km model distance), the velocity profile represents a slightly thickened

491     version of that at 10 km, consistent with the presence of slightly thickened oceanic crust beneath

492     the PMR.  Landward (east) of 60 km model distance (Fig. 9a), the crust thickens and is undoubtedly

493     continental at 80 km. The crustal velocities of P05 (Fig. 9b) and P04 (Fig. 9c) have different trends

494     than those on P06, though the southern part of P04 is poorly constrained.



495
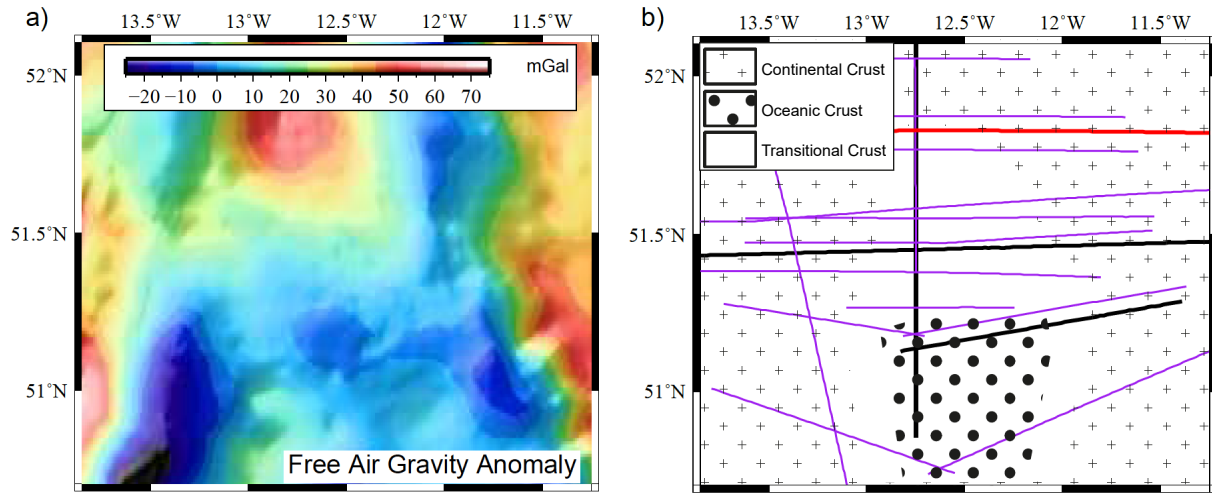
496 **Fig. 10.** (a) The free air gravity anomaly. (b) Interpreted crustal distribution. The red line marks the location of

497 RAPIDS4, and other lines are as in Fig. 1.

498

499     The crustal velocities observed on P06 are similar to those (Fig. 9a) determined in the Porcupine

500     Abyssal Plain on profile COOLE 3B within a thinner oceanic crust, but much higher than those

501     towards the mouth of the Porcupine Seabight which has a similar crustal thickness [*Makris et al.*,

502     1988]. Based on COOLE 3A and 3B data, the structure in this region comprises an upper crust of

503     5.9 - 6.1 km/s and a lower crust of 6.4 - 6.6 km/s, which were interpreted as continental crust, with

504     an 8 km/s upper mantle. Velocities on P06 are also very close to the oceanic crustal velocities

505     modelled from wide-angle seismic data with a similar strategy in the Gulf of Cadiz, where

506     lithosphere of similar age is inferred [*Sallarès et al.*, 2013]. The velocity-depth profiles beneath

507     the PMR show a similar velocity range, but with a thicker layer 3. This slightly thicker layer 3 can

508     be attributed to additional magmatism during the formation of the PMR. The velocity trends here

509     are similar to those of thickened oceanic crust modeled from OBS data in Hatton Bank [*Fowler et*

510    *al.*, 1989] and Greenland [*Hopper et al.*, 2003]. However, the crust in Hatton Bank and Greenland

511    are much thicker, interpreted as resulting from the effects of the Iceland plume.

512

513    Many North Atlantic continental margins, for example, Carolina Trough [*Tréhu et al.*, 1989],

514    Hatton Bank [*Fowler et al.*, 1989] and the East Greenland margin [*Hopper et al.*, 2003], have been

515    observed to have lower crustal velocities > 7 km/s that are interpreted as underplated or

516    magmatically-intruded continental crust. SDRs (seaward dipping reflectors) have been commonly

517    observed from seismic reflection data at these margins. However, no evidence suggesting the

518    existence of SDRs has been identified on seismic reflection profiles from the Porcupine Basin.

519    Therefore, our velocity model for P06 is unlikely to represent a volcanic continental margin.

520    Finally, the crust modelled from RAPIDS4 (location in Fig. 10b) further north in the Porcupine

521    Basin [*O'Reilly et al.*, 2006] exhibits much lower velocities (6.0 – 6.5 km/s), providing further

522    support for the suggestion that the crust in the western part of P06 very likely to be oceanic in

523    nature (Fig. 10b).

524

525    Seismic reflection data (profile 138) show that the central part of the basin has a smooth top

526    basement morphology and a lack of tilted fault blocks and no evidence for pre-rift sediments (Fig.

527    6e). This morphology provides further evidence for the absence of thinned continental crust at the

528    western part of P06 (< 60 km). An oceanic nature of the crust (Fig. 10b) in the southern Porcupine

529    Basin is compatible with the approach we applied for the gravity modelling (Fig. 8a, c). In addition,

530    the depleted nature of oceanic mantle can result in a greater density than for continental mantle

531    [*Jordan*, 1988].

532    6.1.2 Age of the interpreted oceanic crust

533    Drilling (well 43/13-1) into a syn-rift sedimentary unit suggests that the post-rift sequence may

534    start in the Berriasian, but it cannot provide the exact age of the onset of rifting. Thus, we speculate

535    that the youngest possible age for the oceanic crust is perhaps latest Tithonian, and it cannot be

536    older than Upper Jurassic. During this period, the frequent reversal of a weak magnetic field

537    [*Steiner et al., 1998*], known as the "Jurassic Quiet Zone" [*Larson and Hilde*, 1975] would explain

538    the absence of clear linear magnetic anomalies in the Porcupine Basin. Alternatively, the thick

539    Cretaceous sedimentary sequence suggests a high sedimentation rate, and possibly the rapid

540  blanketing by sediments caused sufficiently high temperatures within layer 2 that the basalts lost

541  much of their initial magnetization through low grade metamorphism, as observed in several

542  Mediterranean basins [*Vogt et al.*, 1971] and in Baffin Bay [*Keen and Barrett*, 1972].

543  6.2 Northern Porcupine Basin

544  Crystalline continental crust (5.7 - 6.5 km/s) was observed at < 100 km along P04 (Fig. 4a),

545  exhibiting typical continental velocity structure [*Christensen*, 1995]. A southward decrease in

546  crustal thickness and a maximum crustal stretching factor βc >10 at ~120 km suggests

547  hyperextension of continental crust and even potentially crustal break-up towards the south of the

548  Porcupine Basin, as well as mantle serpentinization beneath the Porcupine Arch [*Prada et al.*,

549  2017]. At > 100 km along P04, southward thinning of the crust ceases. Furthermore, in seismic

550  reflection data, the top of basement approaches the two-way time of the Moho inferred from wide-

551  angle data (Fig. 6b). A clear expression of the Porcupine Arch (or "P") disappears, and there is a

552  change in the sedimentary infill (Fig. 2b). Thus, we suggest that the southern limit of continental

553  crust occurs at this location (Fig. 10b).

554

555  Extended continental crust and unambiguous oceanic crust are commonly separated by a zone of

556  transition, generally referred to as the continent-ocean transition (COT) [*Whitmarsh and Miles*,

557  1995; *Peron-Pinvidic et al.*, 2013]. Above the Moho, much of the basement on P05 is characterized

558  by high velocity gradients underlain by lower gradients, (Fig. 9b) and velocity-depth profiles

559  encroach on those of exhumed and serpentinized mantle [*Minshull*, 2009], particularly toward the

560  rift axis (160 - 170 km). The velocity structure may suggest the possible presence of partially

561  serpentinized mantle with a downward decrease in the degree of serpentinization.  However, these

562  basement velocities would also match well a ~4 km thick oceanic crust. Moving away from the

563  rift axis (< 120 km and > 190 km), the velocity structure becomes typically continental, and the

564  basement is much thicker.

565

566  At > 100 km model distance along P04, velocity-depth profiles (Fig. 9c) show generally similar

567  velocities to those of exhumed mantle [*Minshull*, 2009] or thin oceanic crust [*White et al.*, 1992].

568  The RAPIDS4 profile (location in Fig. 10b), which crosses P04 at ~110 km, has been modelled

569  with a crustal thickness of around 3 km, and velocities ranging from 5.8 − 6.5 km/s [*O'Reilly et*

570   *al.*, 2006]. This part of the profile has been interpreted as showing thinned continental crust

571   overlaying serpentinized mantle. The difference in velocity between P04 and P05, P06 where they

572   cross is probably due to the major structural changes from north to south along P04. Thus, the

573   TOMO2D inversion finds problems in satisfying all of the data, especially the lateral variations,

574   resulting in a larger velocity uncertainty than for the other two profiles. Differences can be larger

575   than the standard deviations (e.g. Moho depth shown in Fig. 5c and g), emphasising that these

576   plots show relative rather than absolute uncertainties. It is therefore difficult to identify the crustal

577   type confidently in the middle part of P04. However, the deepening of the Moho from 160 km

578   model distance may suggest an increasing thickness of oceanic crust towards the south that is

579   eventually juxtaposed with the oceanic crust observed on P06.  Thus, given the oceanic basement

580   characteristics observed on seismic reflection lines 129 and 144, we interpret the crust at the

581   southern end of P04 and on these profiles to be oceanic (Fig. 10b). Further south, we only have

582   information from the COOLE lines [*Makris et al.*, 1988], where continental crust was inferred on

583   COOLE 3A and the eastern part of COOLE 3B. These profiles are sparsely sampled (12 OBSs on

584   COOLE 3A, but mainly located on the continental shelf and only 5 OBSs on COOLE 3B) and

585   may-merit re-analysis in the light of our observations. However, if we take their interpretation at

586   face value, oceanic crust may be limited to a small region in the center of the basin.

587   6.3 Rift Propagation

588   A set of small basins around Ireland, probably with a NE-SW orientation, started rifting during a

589   Permian to Triassic rifting episode [*Shannon*, 1991; *Naylor and Shannon*, 2009]. Plate

590   reconstructions suggest that the basin underlying the Porcupine Seabight was narrow at that time

591   and adjacent to the East Orphan Basin [*Srivastava and Verhoef*, 1992]. The main rifting episode,

592   from the Late Jurassic to the Early Cretaceous, progressed diachronously from south to north,

593   leading to the E-W separation of the Grand Banks from central Iberia and then to the SE–NW

594   separation of the southeast margin of Flemish Cap from Galicia Bank [*Tucholke et al.*, 2007]. The

595   latter separation was preceded by the opening and subdivision of Orphan Basin [*Sibuet et al.*,

596   2007]. Wide-angle seismic modeling reveals that the East Orphan Basin is underlain by highly

597   stretched continental crust (< 7 km thickness) extending more than 400 km to Orphan Knoll [*Chian*

598   *et al.*, 2001; *Watremez et al.*, 2015]. A similar crustal structure obtained on COOLE 3B [*Makris*

599   *et al.*, 1988] may suggest that the basin underlain the Porcupine Seabight also experienced similar

600  rifting around this time. Thus, it is possible that most of the Porcupine Basin continued rifting and

601  grew based on the original geometry while the southernmost part of the basin went through a

602  similar rifting process to the Orphan Basin. The possible transform fault we observed in the seismic

603  reflection profiles may separate these two regions.

604

605  Based on gravity data, *Readman et al.* [2005] proposed that two transform faults separated the

606  volcanism in the south from the north. In this scenario, a region of narrow segmented sea-floor

607  spreading bounded by NW-SE transform zones may have formed in mid-Late Jurassic-early

608  Cretaceous time.  However, our basement map (Fig. 7b) does not provide strong support for the

609  presence of transform faults at these proposed locations. Alternatively, we propose that the rifting

610  was driven by non-uniform stretching along the rift axis (Fig. 11), with initially more strain focused

611  in the south and therefore more extension there. With the increasing crustal thinning and mantle

612  serpentinization, the mantle eventually become exhumed in the south. This difference in strain

613  may have been caused by an earlier rifting in the south. Then the stretching propagated northward,

614  while at the same time the basin continued opening. This simplified conceptual model explains the

615  structures we observe, comprised of hyperextended continental crust in the north, and oceanic crust

616  in the south, without attempting to address the complicated orientation history of the basin.

617  Southward increasing sedimentary thickness and basement patterns support a northward decrease

618  of extension, and suggest a corresponding increase in lithospheric thickness during rifting. As a

619  natural consequence of rifting, melt would have been generated by mantle decompression. Melt

620  generation focused in the south as more lithospheric thinning occurred here. With continued

621  stretching and opening, regions of magmatic activity developed into seafloor spreading and

622  oceanic crust was accreted.

623

624  Our interpreted rift history has many similarities with that inferred for the Bay of Biscay, which is

625  also a propagating V-shaped ocean basin that opened in the Aptian-Albian time [*Jammes et al.*,

626  2010]. Thus, our analysis sheds further light on the rifting of V-shaped North Atlantic basins

627  [*Péron-Pinvidic and Manatschal*, 2010].
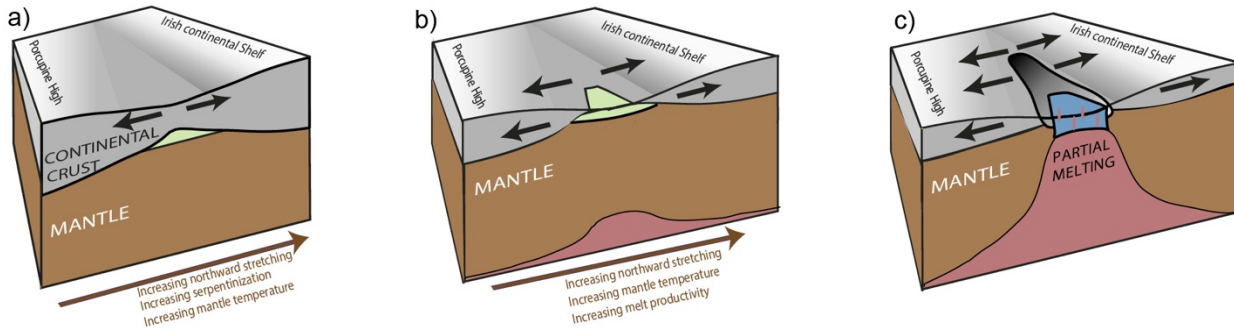
**Fig. 11.** Simplified conceptual model for northward-propagated rifting from magma-poor stretched continental crust to oceanic crust in short distance (adapted from *Shillington et al.* [2009]). Black arrows represent the strain during rifting. Green represents the serpentinization. Blue indicates oceanic crust. Region with gradual change from black to dark grey represents an area of hyper-extended crust with localised mantle exhumation. (a) Main rifting started at Mid-late Jurassic rifting episode. Strain was mainly focused in the south and result in more extension and mantle serpentinization. (b) Along-strike variations in strain leads to northward propagation of rifting and mantle exhumation, as well as a gradual along-strike change in partial melting. (c) Continued rifting and focused magmatic creation in the south leads to incipient seafloor spreading within a narrow region.

## 7 Conclusions

From new wide-angle seismic modelling, we identified three crustal domains in the Porcupine Basin. In the north, continental crust abruptly thins southwards to ~5 km thick. Immediately to the south, there is a zone of which basement is uncertain nature. Further south, we suggest the presence of a 7 − 8 km thick unit of oceanic crust, overlain by a ~ 8 km thick unit of Mesozoic sediments that are covered by 2 km of Cenozoic sediments. Due to a lack of clear magnetic anomalies and of drilling information, we can only constrain limiting ages for the seafloor spreading to the time of the main rifting episode, i.e., Late Jurassic to Early Cretaceous. We propose that the rifting propagated from south to north along the basin axis and was dominated by non-uniform strain. Thus, along-strike variations in crustal and mantle properties are present and stretching eventually led to continental break-up and decompression melting in the southern Porcupine Basin.

## Acknowledgments

660 and Environment, Ireland. Seismic reflection data along SPB97 profiles were supplied by Fugro-
661 Geoteam through Conoco-Phillips. PAD and SPBI98 profiles were provided by the Department of
662 Communications, Climate Action and Environment (Ireland). GMT (Wessel & Smith 1998) was
663 used to prepare all the figures, combined with Seismic-Unix (Stockwell 1999) for some.  TAM
664 was supported by a Wolfson Research Merit award. The wide-angle seismic data used in this study
665 can be accessed via www.pangaea.de.

## References

667 Baxter, K., T. Buddin, D. Corcoran, and S. Smith (2001), Structural modelling of the south Porcupine Basin,
668 offshore Ireland: implications for the timing, magnitude and style of crustal extension, *Geological Society, London,*
669 *Special Publications*, *188*(1), 275-290.
670 Birch, F. (1961), The velocity of compressional waves in rocks to 10 kilobars: 2, *J. Geophys. Res.*, *66*(7), 2199-
671 2224.
672 Boillot, G., G. Feraud, M. Recq, and J. Girardeau (1989), Undercrusting by Serpentinite beneath Rifted Margins,
673 *Nature*, *341*(6242), 523-525.
674 Bullock, A. D., and T. A. Minshull (2005), From continental extension to seafloor spreading: crustal structure of the
675 Goban Spur rifted margin, southwest of the UK, *Geophys. J. Int.*, *163*(2), 527-546.
676 Bulois, C., P. Shannon, P. Manuel, C.-R. Nicolas, W. Louise, and D. Jacques (2017), Multiphased extension along
677 continental margins: a case study of the Porcupine Basin, offshore Ireland, paper presented at *19th EGU General*
678 *Assembly, EGU2017, proceedings from the conference held 23-28 April, 2017 in Vienna, Austria., p.9591*9591.
679 Calvès, G., T. Torvela, M. Huuse, and M. G. Dinkleman (2012), New evidence for the origin of the Porcupine
680 Median Volcanic Ridge: Early Cretaceous volcanism in the Porcupine Basin, Atlantic margin of Ireland, *Geochem.*
681 *Geophys. Geosyst.*, *13*(6), 1525-2027.
682 Carlson, R. L., and D. J. Miller (2003), Mantle wedge water contents estimated from seismic velocities in partially
683 serpentinized peridotites, *Geophys. Res. Lett.*, *30*(5), 1944-8007.
684 Chian, D., I. D. Reid, and H. R. Jackson (2001), Crustal structure beneath Orphan Basin and implications for
685 nonvolcanic continental rifting, *J. Geophys. Res.*, *106*(B6), 10923-10940.
686 Christensen, N. I. (1995), Seismic velocity structure and composition of the continental crust: A global view, *J.*
687 *Geophys. Res.*, *100*(B7), 9761-9788.
688 Fowler, S., R. White, G. Spence, and G. Westbrook (1989), The Hatton Bank continental margin—II. Deep structure
689 from two-ship expanding spread seismic profiles, *Geophys. J. Int.*, *96*(2), 295-309.
690 Fullea, J., M. R. Muller, A. G. Jones, and J. C. Afonso (2014), The lithosphere–asthenosphere system beneath Ireland
691 from integrated geophysical–petrological modeling II: 3D thermal and compositional structure, Lithos, 189, 49-64.
692 Gagnevin, D., P. D. W. Haughton, L. Whiting, and M. M. Saqab (2017), Geological and geophysical evidence for a
693 mafic igneous origin of the Porcupine Arch, offshore Ireland, *Journal of the Geological Society*.
694 Hamilton, E. L. (1978), Sound velocity–density relations in sea-floor sediments and rocks, *J. Acoust. Soc. Am*,
695 *63*(2), 366-377.
696 Hauser, F., B. O'Reilly, P. Readman, J. Daly, and R. Van den Berg (2008), Constraints on crustal structure and
697 composition within a continental suture zone in the Irish Caledonides from shear wave wide-angle reflection data
698 and lower crustal xenoliths, *Geophys. J. Int.*, *175*(3), 1254-1272.
699 Hopper, J. R., T. Dahl-Jensen, W. S. Holbrook, H. C. Larsen, D. Lizarralde, J. Korenaga, G. M. Kent, and P. B.
700 Kelemen (2003), Structure of the SE Greenland margin from seismic reflection and refraction data: Implications for
701 nascent spreading center subsidence and asymmetric crustal accretion during North Atlantic opening, *J. Geophys.*
702 *Res.*, *108*(B5), 2169-9313.
703 Jammes, S., L. Lavier, and G. Manatschal (2010), Extreme crustal thinning in the Bay of Biscay and the Western
704 Pyrenees: From observations to modeling, *Geochem. Geophys. Geosyst.*, *11*(10).
705 Johnson, H., J. Ritchie, R. Gatliff, J. Williamson, J. Cavill, and J. Bulat (2001), Aspects of the structure of the
706 Porcupine and Porcupine Seabight basins as revealed from gravity modelling of regional seismic transects,
707 *Geological Society, London, Special Publications*, *188*(1), 265-274.
708 Joppen, M., and R. S. White (1990), The structure and subsidence of Rockall Trough from two-ship seismic
709 experiments, *J. Geophys. Res.*, *95*(B12), 0148-0227.
710 Jordan, T. H. (1988), Structure and Formation of the Continental Tectosphere, *JPet*, *Special_Volume*(1), 11-37.
711 Keen, C., and D. Barrett (1972), Seismic refraction studies in Baffin Bay: an example of a developing ocean basin,
712 *Geophys. J. Int.*, *30*(3), 253-271.

713　King, C. (2016), A Revised Correlation of Tertiary Rocks in the British Isles and adjacent areas of NW Europe, in
714　*East Anglia and London Basin (Paleocene and Eocene)*, edited, pp. 329-375, Geological Society of London Special
715　Report.
716　Korenaga, J., and W. W. Sager (2012), Seismic tomography of Shatsky Rise by adaptive importance sampling, *J.*
717　*Geophys. Res.*, *117*(B8).
718　Korenaga, J., R. S. Detrick, and P. B. Kelemen (2001), Gravity anomalies and crustal structure at the southeast
719　Greenland margin, *J. Geophys. Res.*, *106*(B5), 8853-8870.
720　Korenaga, J., W. S. Holbrook, G. M. Kent, P. B. Kelemen, R. S. Detrick, H. C. Larsen, J. R. Hopper, and T. Dahl-
721　Jensen (2000), Crustal structure of the southeast Greenland margin from joint refraction and reflection seismic
722　tomography, *J. Geophys. Res.*, *105*(B9), 21591-21614.
723　Larson, R. L., and T. W. Hilde (1975), A revised time scale of magnetic reversals for the Early Cretaceous and Late
724　Jurassic, *J. Geophys. Res.*, *80*(17), 2586-2594.
725　Lefort, J., and M. Max (1984), Development of the Porcupine Seabight: use of magnetic data to show the direct
726　relationship between early oceanic and continental structures, *Journal of the Geological Society*, *141*(4), 663-674.
727　Makris, J., R. Egloff, A. Jacob, P. Mohr, T. Murphy, and P. Ryan (1988), Continental crust under the southern
728　Porcupine Seabight west of Ireland, *Earth. Planet. Sci. Lett.*, *89*(3), 387-397.
729　Masson, D. G., and P. Miles (1986), Development and hydrocarbon potential of Mesozoic sedimentary basins
730　around margins of North Atlantic, *AAPG Bulletin*, *70*(6), 721-729.
731　McDonnell, A., and P. Shannon (2001), Comparative Tertiary stratigraphic evolution of the Porcupine and Rockall
732　basins, *Geological Society, London, Special Publications*, *188*(1), 323-344.
733　Minshull, T. A. (2009), Geophysical characterisation of the ocean–continent transition at magma-poor rifted
734　margins, *Comptes Rendus Geoscience*, *341*(5), 382-393.
735　Moore, J., and P. Shannon (1995), The Cretaceous succession in the Porcupine Basin, offshore Ireland: facies
736　distribution and hydrocarbon potential, *Geological Society, London, Special Publications*, *93*(1), 345-370.
737　Moser, T. (1991), Shortest path calculation of seismic rays, *Geophys.*, *56*(1), 59-67.
738　Moser, T. J., G. Nolet, and R. Snieder (1992), Ray Bending Revisited, *Bull. Seismol. Soc. Am.*, *82*(1), 259-288.
739　Naylor, D., and P. Shannon (2009), Geology of offshore Ireland, in *The geology of Ireland, Dunedin Academic*
740　*Press*, edited by C. H. Holland, pp. 405-460, Edinburgh.
741　Naylor, D., P. M. Shannon, and N. Murphy (2002), Porcupine-Goban Region: A Standard Structural Nomenclature
742　System, edited, p. 65, Petroleum Affairs Division, Special Publications, 1/02.
743　O'Reilly, B., F. Hauser, C. Ravaut, P. Shannon, and P. Readman (2006), Crustal thinning, mantle exhumation and
744　serpentinization in the Porcupine Basin, offshore Ireland: evidence from wide-angle seismic data, *Journal of the*
745　*Geological Society*, *163*(5), 775-787.
746　O'Reilly, B. M., F. Hauser, A. B. Jacob, and P. M. Shannon (1996), The lithosphere below the Rockall Trough:
747　wide-angle seismic evidence for extensive serpentinisation, *Tectonophysics*, *255*(1), 1-23.
748　Paige, C. C., and M. A. Saunders (1982), LSQR: An algorithm for sparse linear equations and sparse least squares,
749　*ACM transactions on mathematical software*, *8*(1), 43-71.
750　Perez-Gussinye, M., and T. J. Reston (2001), Rheological evolution during extension at nonvolcanic rifted margins:
751　Onset of serpentinization and development of detachments leading to continental breakup, *J. Geophys. Res.*,
752　*106*(B3), 3961-3975.
753　Peron-Pinvidic, G., G. Manatschal, and P. T. Osmundsen (2013), Structural comparison of archetypal Atlantic rifted
754　margins: a review of observations and concepts, *Mar. Pet. Geol.*, *43*, 21-47.
755　Péron-Pinvidic, G., and G. Manatschal (2010), From microcontinents to extensional allochthons: witnesses of how
756　continents rift and break apart?, *Petroleum Geoscience*, *16*(3), 189-197.
757　Planke, S. (1994), Geophysical response of flood basalts from analysis of wire line logs: Ocean Drilling Program
758　Site 642, Vøring volcanic margin, *J Geophys Res*, *99*(B5), 9279-9296.
759　Prada, M., L. Watremez, C. Chen, B. M. O'Reilly, T. A. Minshull, T. J. Reston, P. M. Shannon, D. Klaeschen, G.
760　Wagner, and V. Gaw (2017), Crustal strain-dependent serpentinisation in the Porcupine Basin, offshore Ireland,
761　*Earth. Planet. Sci. Lett.*, *474*, 148-159.
762　Praeg, D., M. Stoker, P. Shannon, S. Ceramicola, B. Hjelstuen, J. Laberg, and A. Mathiesen (2005), Episodic
763　Cenozoic tectonism and the development of the NW European 'passive'continental margin, *Mar. Pet. Geol.*, *22*(9),
764　1007-1030.
765　Readman, P., B. O'Reilly, J. Edwards, and M. Sankey (1995), A gravity map of Ireland and surrounding waters,
766　*Geological Society, London, Special Publications*, *93*(1), 9-16.

767 Readman, P. W., B. M. O'Reilly, P. M. Shannon, and D. Naylor (2005), The deep structure of the Porcupine Basin,
768 offshore Ireland, from gravity and magnetic studies, *Geological Society, London, Petroleum Geology Conference*
769 *Series.*, *6*(1), 1047-1056.
770 Reston, T., J. Pennell, A. Stubenrauch, I. Walker, and M. Perez-Gussinye (2001), Detachment faulting, mantle
771 serpentinization, and serpentinite-mud volcanism beneath the Porcupine Basin, southwest of Ireland, *Geology*,
772 *29*(7), 587-590.
773 Reston, T. J. (2009), The structure, evolution and symmetry of the magma-poor rifted margins of the North and
774 Central Atlantic: A synthesis, *Tectonophysics*, *468*(1-4), 6-27.
775 Reston, T. J., V. Gaw, J. Pennell, D. Klaeschen, A. Stubenrauch, and I. Walker (2004), Extreme crustal thinning in
776 the south Porcupine Basin and the nature of the Porcupine Median High: implications for the formation of non-
777 volcanic rifted margins, *J Geol Soc London*, *161*(5), 783-798.
778 Sallarès, V., A. Gailler, M.-A. Gutscher, D. Graindorge, R. Bartolomé, E. Gràcia, J. Díaz, J. J. Dañobeitia, and N.
779 Zitellini (2011), Seismic evidence for the presence of Jurassic oceanic crust in the central Gulf of Cadiz (SW Iberian
780 margin), *Earth. Planet. Sci. Lett.*, *311*(1), 112-123.
781 Sallarès, V., S. Martínez-Loriente, M. Prada, E. Gràcia, C. Ranero, M.-A. Gutscher, R. Bartolome, A. Gailler, J. J.
782 Dañobeitia, and N. Zitellini (2013), Seismic evidence of exhumed mantle rock basement at the Gorringe Bank and
783 the adjacent Horseshoe and Tagus abyssal plains (SW Iberia), *Earth. Planet. Sci. Lett.*, *365*, 120-131.
784 Shannon, A. McDonnell, and W. Bailey (2007), The evolution of the Porcupine and Rockall basins, offshore
785 Ireland: the geological template for carbonate mound development, *Int J Earth Sci*, *96*(1), 21-35.
786 Shannon, P. M. (1991), The development of Irish offshore sedimentary basins, *Journal of the Geological Society*,
787 *148*(1), 181-189.
788 Shannon, P. M., D. Corcoran, and P. Haughton (2001), The petroleum exploration of Ireland's offshore basins:
789 introduction, *Geological Society, London, Special Publications*, *188*(1), 1-8.
790 Shillington, D. J., C. L. Scott, T. A. Minshull, R. A. Edwards, P. J. Brown, and N. White (2009), Abrupt transition
791 from magma-starved to magma-rich rifting in the eastern Black Sea, *Geology*, *37*(1), 7-10.
792 Sibuet, J.-C., S. Srivastava, M. Enachescu, and G. Karner (2007), Early Cretaceous motion of Flemish Cap with
793 respect to North America: implications on the formation of Orphan Basin and SE Flemish Cap–Galicia Bank
794 conjugate margins, *Geological Society, London, Special Publications*, *282*(1), 63-76.
795 Spudich, P., and J. Orcutt (1980), A new look at the seismic velocity structure of the oceanic crust, *Rev. Geophys.*,
796 *18*(3), 627-645.
797 Srivastava, S., and J. Verhoef (1992), Evolution of Mesozoic sedimentary basins around the North Central Atlantic:
798 a preliminary plate kinematic solution, *Geological Society, London, Special Publications*, *62*(1), 397-420.
799 Steiner, C., A. Hobson, P. Favre, G. M. Stampfli, and J. Hernandez (1998), Mesozoic sequence of Fuerteventura
800 (Canary Islands): Witness of Early Jurassic sea-floor spreading in the central Atlantic, *GSAMB*, *110*(10), 1304-1317.
801 Tate, M. (1992), The Clare Lineament: a relic transform fault west of Ireland, *Geological Society, London, Special*
802 *Publications*, *62*(1), 375-384.
803 Tate, M. (1993), Structural framework and tectono-stratigraphic evolution of the Porcupine Seabight Basin, offshore
804 western Ireland, *Mar. Pet. Geol.*, *10*(2), 95-123.
805 Tate, M., and M. Dobson (1988), Syn-and post-rift igneous activity in the Porcupine Seabight Basin and adjacent
806 continental margin W of Ireland, *Geological Society, London, Special Publications*, *39*(1), 309-334.
807 Tate, M., N. White, and J. J. Conroy (1993), Lithospheric Extension and Magmatism in the Porcupine Basin West of
808 Ireland, *J. Geophys. Res.*, *98*(B8), 13905-13923.
809 Tréhu, A. M., A. Ballard, L. Dorman, J. Gettrust, K. Klitgord, and A. Schreiner (1989), Structure of the lower crust
810 beneath the Carolina Trough, US Atlantic continental margin, *J Geophys Res*, *94*(B8), 10585-10600.
811 Tucholke, B., D. Sawyer, and J.-C. Sibuet (2007), Breakup of the Newfoundland–Iberia rift, *Geological Society,*
812 *London, Special Publications*, *282*(1), 9-46.
813 Vogt, P., R. Higgs, and G. Johnson (1971), Hypotheses on the origin of the Mediterranean basin: magnetic data, *J.*
814 *Geophys. Res.*, *76*(14), 3207-3228.
815 Watremez, L., K. W. H. Lau, M. R. Nedimovic, and K. E. Louden (2015), Traveltime tomography of a dense wide-
816 angle profile across Orphan Basin, *Geophys.*, *80*(3), B69-B82.
817 Watremez, L., M. Prada, T. Minshull, B. O'Reilly, C. Chen, T. Reston, P. Shannon, G. Wagner, V. Gaw, D.
818 Klaeschen, R. Edwards, and S. Lebedev (2016), Deep structure of the Porcupine Basin from wide-angle seismic
819 data, in Bowman, M. and B. Levell (Eds), *Petroleum Geology of NW Europe: 50 Years of Learning – Proceedings*
820 *of the 8th Petroleum Geology Conference,* doi:10.1144/PGC8.26, Geological Society, London
821 White, R. S., D. Mckenzie, and R. K. Onions (1992), Oceanic Crustal Thickness from Seismic Measurements and
822 Rare-Earth Element Inversions, *J. Geophys. Res.*, *97*(B13), 19683-19715.

823   White, R. S., et al. (2008), Lower-crustal intrusion on the North Atlantic continental margin, *Nature*, *452*(7186),
824       460-464.
825   Whitmarsh, R. B., and P. R. Miles (1995), Models of the development of the West Iberia rifted continental margin at
826       40° 30′ N deduced from surface and deep-tow magnetic anomalies, *J Geophys Res*, *100*(B3), 3789-3806.
827   Zelt, C., and D. Forsyth (1994), Modeling wide-angle seismic data for crustal structure: Southeastern Grenville
828       Province, *J Geophys Res*, *99*(B6), 11687-11704.
829   Zelt, C. A. (1998), Lateral velocity resolution from three-dimensional seismic refraction data, *Geophys. J. Int.*,
830       *135*(3), 1101-1112.
831   Zelt, C. A., and R. B. Smith (1992), Seismic traveltime inversion for 2-D crustal velocity structure, *Geophys. J. Int.*,
832       *108*(1), 16-34.
833